Matter

CellPress

Article

Stretchable hybrid response pressure sensors

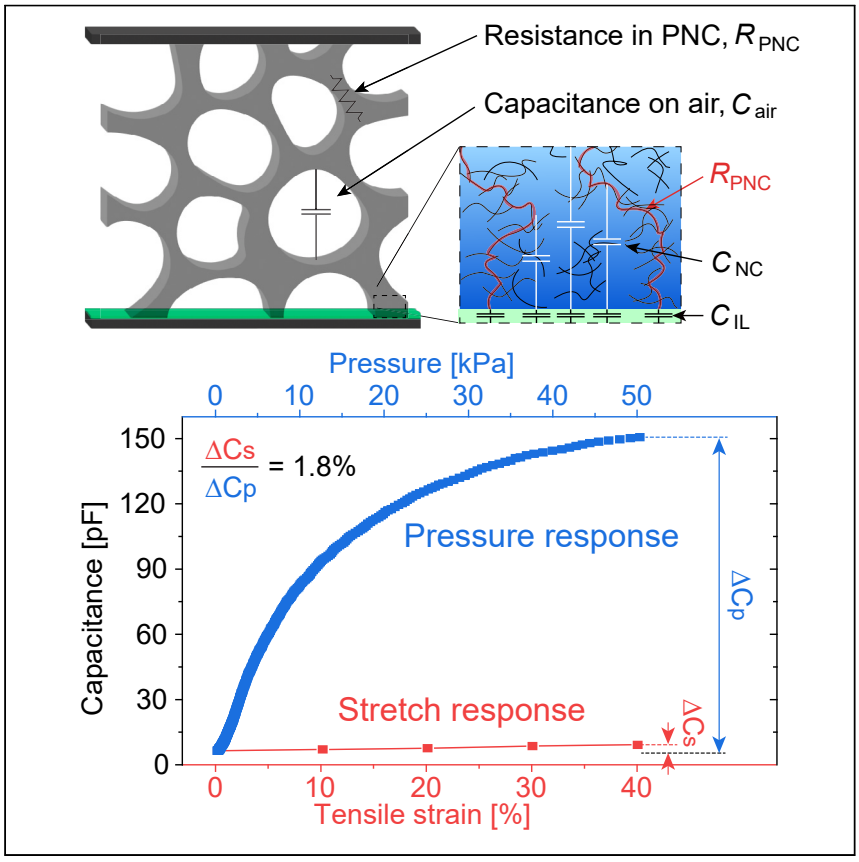

The SHRPS comprises a barely conductive porous nanocomposite (PNC) and an ultrathin insulating layer sandwiched between two electrodes. During stretching, the resistance of the PNC remains high, making capacitance the dominant factor in determining the sensor's output signal. Conversely, when pressure is applied, the collapse of air pores in the foam leads to a decrease in resistance, thereby dominating the output signal. This distinct mechanism allows SHRPSs to differentiate between stretch and pressure responses.

Kyoung-Ho Ha, Zhengjie Li, Sangjun Kim, ..., Charles Block, Sarnab Bhattacharya, Nanshu Lu

nanshulu@utexas.edu

Highlights

Hybrid piezoresistivity and piezocapacitivity allow accurate pressure measurement

Hybrid response occurs under pressure, while capacitive response occurs under stretch

Optimal CNT doping ratio in PNC achieves highest pressure sensitivity of SHRPS

Analytical models show SHRPS is governed by a new mechanism, not material properties

1 **Discovery**
A new material or phenomena

Ha et al., Matter 7, 1895–1908
May 1, 2024
https://doi.org/10.1016/j.matt.2024.04.009

Matter

CellPress

Article

Stretchable hybrid response pressure sensors

Kyoung-Ho Ha,[1,6] Zhengjie Li,[2] Sangjun Kim,[1] Heeyong Huh,[2] Zheliang Wang,[2] Hongyang Shi,[3] Charles Block,[3,7] Sarnab Bhattacharya,[3] and Nanshu Lu[1,2,3,4,5,8,*]

SUMMARY

Touch-sensitive stretchable electronic skins (e-skins) hold promise for soft robots, prosthetics, bio-mimetics, and bio-sensors. However, a long-standing challenge has been the interference of stretching in pressure readings. Addressing this, we introduce an intrinsically stretchable hybrid response pressure sensor (SHRPS) composed of a laminate featuring a barely conductive porous nanocomposite and an ultrathin dielectric layer situated between two stretchable electrodes. The combined piezoresistive and piezocapacitive responses of the SHRPS enable ultrahigh pressure sensitivity while effectively negating stretch-induced interference. Our findings are underpinned by an experimentally validated electromechanical model. In practical applications, SHRPS mounted on inflatable probes demonstrated safe and precise palpation on the human wrist and conformable and firm gripping of contoured objects. The debut of SHRPS promises to significantly expand the versatile applications of e-skins.

INTRODUCTION

Electronic skins (e-skins), which mimic the properties and functionalities of human skin, particularly its softness and tactile sensation, are essential for a variety of technologies such as soft robots, prosthetics, bio-mimetics, and bio-sensors.[1–5] As a central component of e-skins, soft pressure sensors have been the subject of extensive research for decades. Among the different types of pressure sensors, including piezoresistive, piezoelectric, triboelectric, ionic, optical, and magnetic ones, capacitive pressure sensors (CPSs) have gained popularity due to their high sensitivity, superior repeatability and stability, softness, and simple construction.[6–12] Recent advances in soft CPSs include higher sensitivity,[13] wider sensing ranges,[14] more linear responses,[15] shear differentiation,[16] transparency,[17] degradability,[18] and imperceptibility when worn by humans.[19] However, stretchability, particularly accurate pressure reading under stretch, has been widely investigated but is still not fully achieved.[20] Stretchable pressure sensors are necessary for covering non-developable and/or highly deformable surfaces. Precise pressure sensing under stretch can significantly enhance the force perception of highly deformable soft robots[21] or wearable haptic devices[22] or enable the accurate detection of pressure exerted on curvilinear and stretchable human skin due to, for example, contact with prostheses,[23] bedding,[24] or shoes.[25]

Technically, stretchable CPSs can be manufactured by sandwiching stretchable dielectric materials between stretchable electrodes.[26–28] However, after many material and structural innovations,[29] there still exists an intrinsic bottleneck—the capacitance output is sensitive to both in-plane stretch and out-of-plane pressure.[26,30] When subjected to stretch, both the enlarged electrode area and

PROGRESS AND POTENTIAL

Accurate pressure measurement holds critical importance across various fields such as soft robotics, bio-mimetics, and biosensors, where surfaces are subject to stretching. Despite considerable advancements in material and structural innovations enabling the fabrication of stretchable pressure sensors, a significant challenge persists: these sensors exhibit sensitivity to both in-plane stretch and out-of-plane pressure, rendering them inaccurate when subjected to simultaneous stretch and pressure. To address this challenge, we introduce intrinsically stretchable hybrid response pressure sensors (SHRPSs), which boast ultrahigh pressure sensitivity while effectively mitigating stretch-induced interference. The introduction of SHRPSs marks a significant milestone, poised to greatly enhance the versatility of electronic skin applications.

reduced inter-electrode gap due to the Poisson's effect of the dielectric lead to an increase in capacitance. If pressure is applied simultaneously, it is impossible to discriminate the source of capacitance change, and hence the capacitance change cannot provide accurate pressure reading under stretch. There exist a few engineering strategies to circumvent this predicament, including stiff-island-enabled strain isolation[31,32] or capacitance compensation based on independent strain sensors.[26,27] However, intrinsically stretchable and accurate CPS without resolution-limiting islands or extra strain-sensing channels are much more desirable but not yet available.

RESULTS AND DISCUSSION

We present an intrinsically stretchable CPS that is marginally sensitive to stretch but immensely sensitive to pressure due to its hybrid piezoresistive and piezocapacitive responses under compression. This stretchable hybrid response pressure sensor (SHRPS) consists of four intrinsically stretchable layers—top and bottom electrodes of carbon nanotube (CNT)-embedded polydimethylsiloxane (PDMS), one barely conductive porous nanocomposite (PNC), and one ultrathin PDMS dielectric layer inserted between the PNC and the bottom electrode (Figure 1A). The detailed fabrication process is described in the experimental procedures and Figure S1. The PNC has an open cell structure with CNT-doped Ecoflex ligaments and 82% porosity (Figure 1B, left), giving rise to piezoresistivity and dispersed parasitic capacitance in the PNC. The PNC is stretchable up to 70% due to both the porous structure and the intrinsically stretchable ligaments (Figure 1B, right). The PNC is 1 mm thick, and the overall thickness of the SHRPS is 1.3 mm (see Figure S2).

The SHRPS operates through a distinct mechanism from conventional CPSs, which can be understood through the conceptual electromechanical simulation (details in the experimental procedures) results displayed in Figures 1C and S3. Figure 1C segments prior CPSs into two categories: engineered dielectrics (Figure 1Ci) and engineered electrodes (Figure 1Ciii). It highlights that SHRPSs (Figure 1Cii), while exhibiting traits common to both categories, also stand distinct from each. Specifically, when relaxed and stretched, the SHRPS's electric field mirrors that of CPSs with engineered dielectrics; conversely, when compressed, it aligns more with the behavior of compressed CPSs with engineered electrodes. The transition from dielectric-like PNC in the undeformed state to electrode-like PNC in the compressed state is accompanied by large changes in both resistance and capacitance, which synergistically gives rise to the unprecedented high pressure sensitivity in SHRPSs. Expanded discussions of Figure 1C are available in supplemental experimental procedures 1. Equivalent circuits for the quantitative analysis of the three different types of CPSs are offered later in this paper. While there is abundant literature reporting CPSs with structured dielectrics[33] and structured electrodes,[34] SHRPSs are new, and understanding their responses to pressure and stretch is the focus of this work.

The SHRPS is stretchable up to 70% both uniaxially and biaxially (Figure S4). The stretch-induced resistance change of CNT-embedded PDMS electrodes has been characterized and proved to be irrelevant to the capacitance readings of the SHRPS (Figure S5). The initial compressive modulus of the SHRPS was measured to be 1 kPa (Figure S6). As shown in Figure 1D, sandwiching a single intact piece of PNC laminated with an ultrathin blanket layer of PDMS dielectric by two orthogonal arrays of parallel electrodes forms a 3 × 3 array of SHRPSs that is soft enough to be stretched, bent, and twisted.

[1]Department of Mechanical Engineering, University of Texas at Austin, Austin, TX 78712, USA

[2]Department of Aerospace Engineering and Engineering Mechanics, University of Texas at Austin, Austin, TX 78712, USA

[3]Department of Electrical and Computer Engineering, University of Texas at Austin, Austin, TX 78712, USA

[4]Department of Biomedical Engineering, University of Texas at Austin, Austin, TX 78712, USA

[5]Texas Materials Institute, University of Texas at Austin, Austin, TX 78712, USA

[6]Present address: Querrey Simpson Institute for Bioelectronics, Northwestern University, Evanston, IL 60208, USA

[7]Present address: Department of Computer Science, University of Illinois at Urbana-Champaign, Champaign, IL 61820, USA

[8]Lead contact

*Correspondence: nanshulu@utexas.edu

https://doi.org/10.1016/j.matt.2024.04.009

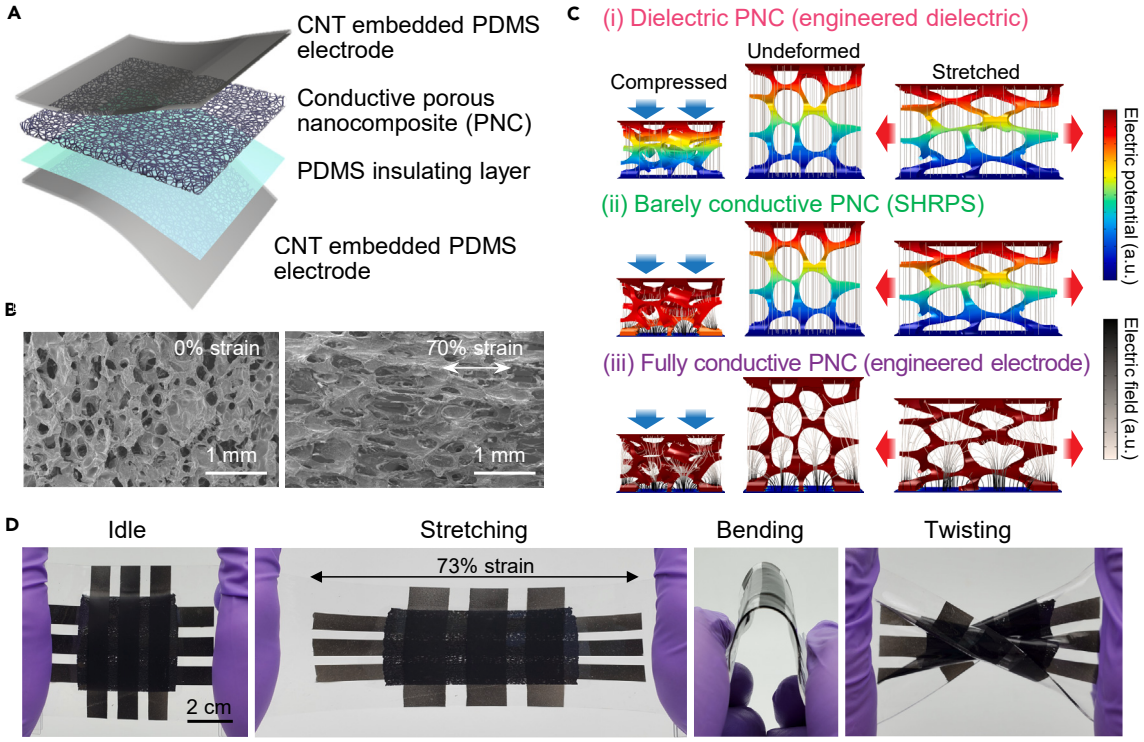

Figure 1. Overview of SHRPS structure, mechanism, and stretchability

(A) Schematic representation of the different layers in a stretchable hybrid response pressure sensor (SHRPS).

(B) Scanning electron microscope images of a PNC before and after undergoing 70% uniaxial tensile strain.

(C) Depiction of the electric potential (color contours) and electric field (streamlines) in three different types of CPSs in undeformed (middle), compressed (left), and stretched (right) states.

(D) A 3 × 3 array of SHRPSs under idle, stretching, bending, and twisting.

Pressure vs. stretch responses

SHRPS performance can be best appreciated through comparison with conventional CPSs. We fabricated and characterized CPSs with three different types of pressure sensing layers: solid Ecoflex, porous Ecoflex, and barely conductive PNC (SHRPS), as illustrated in the first row of Figure 2. Their capacitance changes were measured when the sensors were subjected to in-plane stretch up to 40% and out-of-plane pressure up to 50 kPa, both separately (the second row of Figure 2) and simultaneously (the third row of Figure 2). The ranges of pressure[35] and tensile strain[36] were chosen based on the values that human skins generally experience.

The CPS with solid Ecoflex has lower pressure sensitivity than its porous counterpart (see blue markers in Figures 2Aii vs. 2Bii). This is due to the higher mechanical stiffness and lower dielectrostriction (i.e., the variation of dielectric constant with pressure) in the solid layer.[7] In contrast, when subjected to pure stretch, both sensors display a linear capacitance-strain relationship (red markers in Figures 2Aii, 2Bii, and S7), as theoretically expected (supplemental experimental procedures 2-1). When both stretch and pressure are applied concurrently, interference from stretching is evident in both instances. However, it is notably less pronounced in the porous Ecoflex CPS (Figure 2Biii) than in the solid Ecoflex CPS (Figure 2Aiii).

In contrast, the SHRPS in Figure 2C exhibits markedly higher pressure sensitivity than those in Figures 2A and 2B, revealing hybrid piezoresistive and piezocapacitive

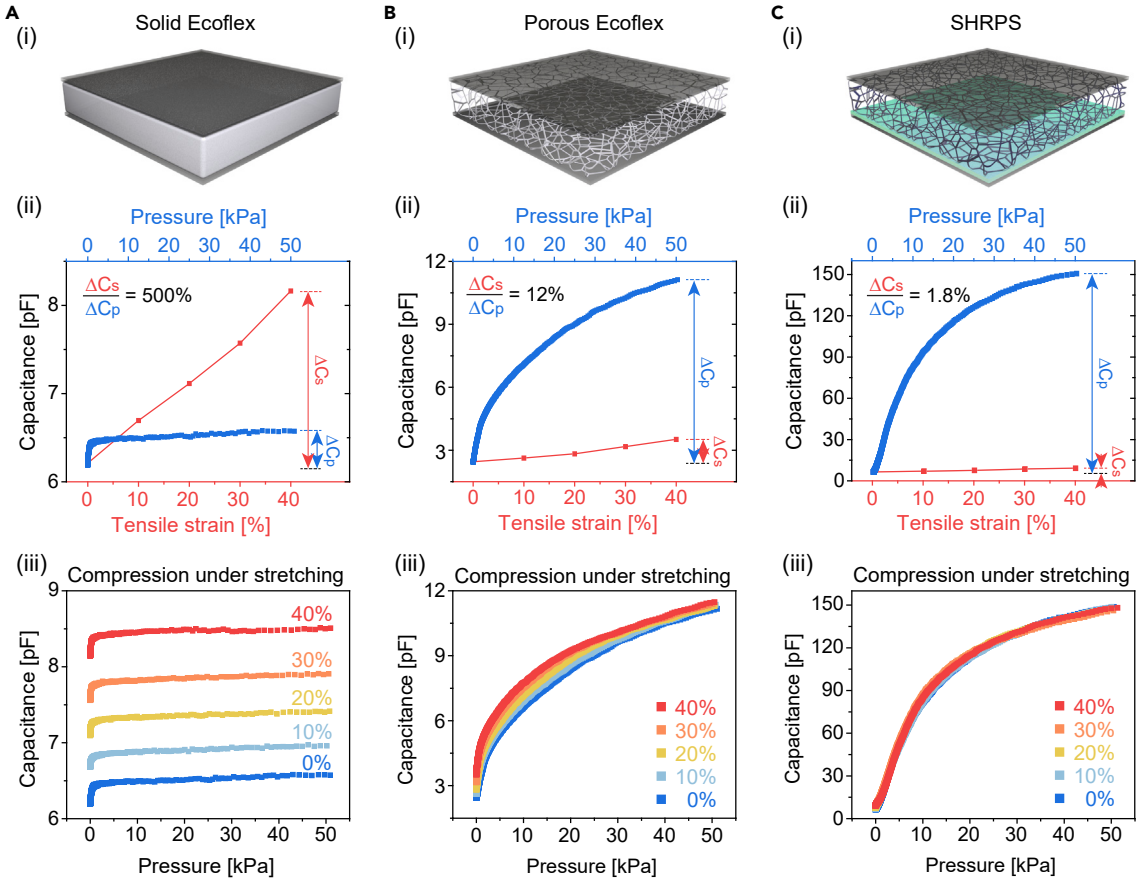

Figure 2. Pressure and stretch responses of a CPS with three different types of pressure sensing materials

(A) Solid Ecoflex.

(B) Porous Ecoflex.

(C) Barely conductive PNC, which is the case of SHRPS.

(Ai, Bi, and Ci) Schematics. (Aii, Bii, and Cii) Pressure (blue) and stretch (red) were applied separately. (Aiii, Biii, and Ciii) Pressure and stretch were applied simultaneously.

responses under pressure. Its stretch response, however, is dominated by the capacitance of the PNC, as uncompressed PNC resistance far exceeds its reactance (Figure S8). Thus, the SHRPS mirrors a conventional CPS under stretch. Consequently, pressure effects overwhelm stretch effects in SHRPSs (Figure 2Cii). When both are applied, the pressure response curves under various tensile strains almost fully overlap in Figure 2Ciii.

Electromechanical characterization of PNC and SHRPS

The piezoresistivity of PNCs plays a key role in the pressure sensitivity of SHRPSs, which can be tuned by the CNT doping ratio in the PNC. An increase in CNT doping ratio leads to a reduction in the PNC initial resistance (Figure 3A). Upon compression, the PNC resistance decreases by orders of magnitude due to the enhanced electrode-PNC contacts as well as self-contact within PNC ligaments, which also close air pores and increase the capacitance of the PNC. The absolute capacitance of the SHRPS increases monotonically with the CNT content and pressure (Figure S9). However, regarding normalized capacitance change and sensitivity, the largest doping is not the optimum one (Figure 3B). This is because the increase in CNT content would increase the initial capacitance of the undeformed SHRPS (Figure S10)

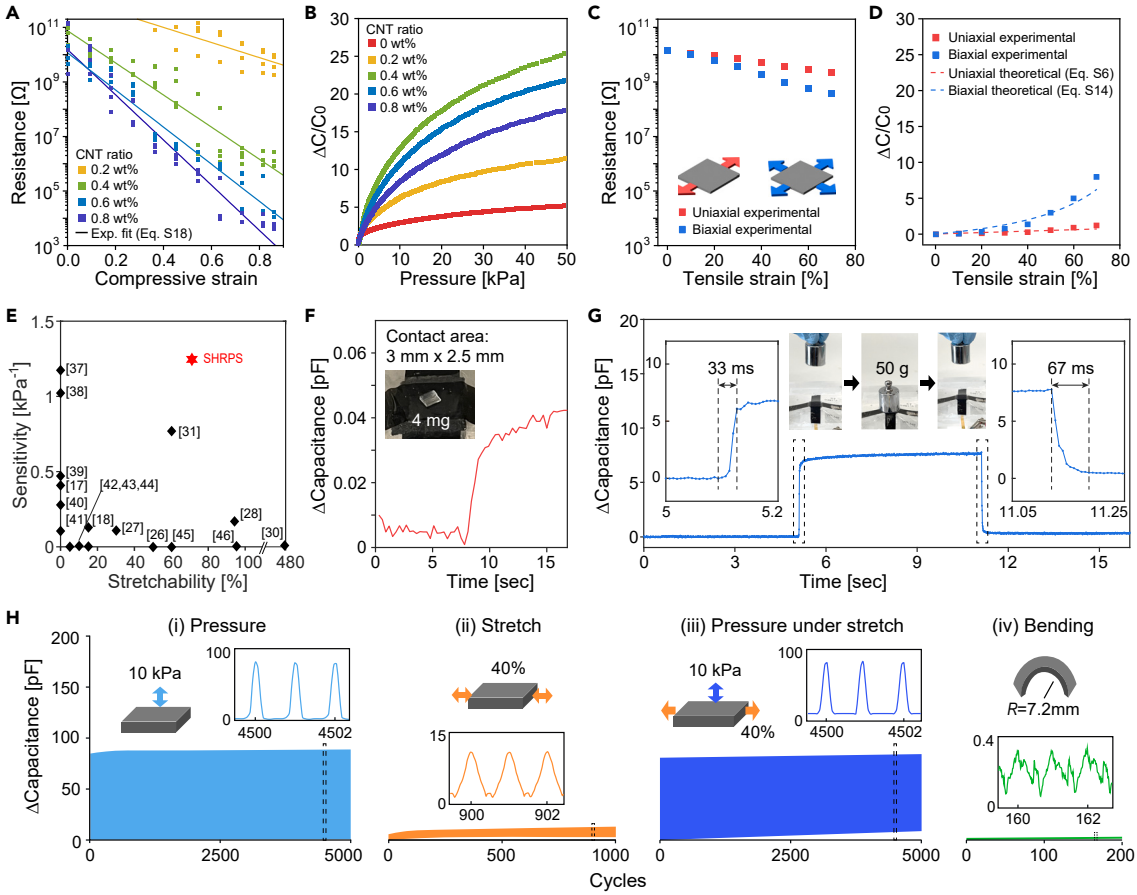

Figure 3. Electromechanical characterization of PNCs and SHRPSs

(A) Resistance changes of PNC with various CNT doping ratios under compression.

(B) Normalized capacitance changes of SHRPS under pressure.

(C) Resistance changes of PNC with 0.4 wt % CNT under uniaxial and biaxial tensile strains.

(D) Normalized capacitance changes of SHRPS with 0.4 wt % CNT under uniaxial and biaxial tensile strains.

(E) Ashby plot comparing the pressure sensitivity (0–10 kPa range) and stretchability of SHRPSs with existing CPSs.

(F) Lowest limit of detectable pressure of SHRPS.

(G) Response and recovery times of SHRPS.

(H) Repeatability and durability tests of SHRPS under (i) 0–10 kPa pressure, (ii) 0%–40% uniaxial tensile strain, (iii) 0–10 kPa pressure under a constant uniaxial tensile strain of 40%, and (iv) bending from flat state to 7.2 mm radius.

and also affects the piezocapacitivity. The sample with the 0.4 wt % CNT (green curve) exhibits the highest sensitivity among the five different doping ratios we studied, with sensitivities of 2.13 kPa^{-1} within 0 and 1 kPa, 1.55 kPa^{-1} within 1 and 5 kPa, 0.82 kPa^{-1} within 5 and 10 kPa, 0.42 kPa^{-1} within 10 and 30 kPa, and 0.21 kPa^{-1} within 30 and 50 kPa. The SHRPS with the 0.4 wt % CNT remains sensitive up to 300 kPa (Figure S11). A quantitative understanding of the optimal CNT content is achieved through an analytical model in the next section.

The electromechanical behaviors of the PNC and SHRPS under stretch are substantially different from those under pressure. Focusing on the PNC with the 0.4 wt % CNT, the initial resistance of 33.2 GΩ decreases to 2.19 MΩ under 70% compression (Figure 3A) but only to 2.21 GΩ under 70% tensile strain (Figure 3C). Considering the limited impact of stretching on PNC resistance, the change in SHRPS capacitance primarily results from PNC capacitance changes during

stretching, which are considerably minor (Figure 3D) in contrast to those induced by pressure (Figure 3B). As expected by the analytical models (dashed curves in Figure 3D and details in supplemental experimental procedures 2), biaxial strains have larger effects than uniaxial strains, which could be a source of error when gentle pressure is accompanied by excessive biaxial stretch. Comparing the performance of SHRPSs with other existing CPSs, the SHRPS shows an unprecedented combination of sensitivity (1.25 kPa^{-1} within 0 and 10 kPa) and stretchability (70%), as evidenced in Figure 3E and Table S1.[17,18,26–28,30,31,37–46]

SHRPSs can detect subtle pressures as low as 5.22 Pa (Figure 3F), which matches well with the pressure detection limit of human skins.[47] SHRPS response and recovery times are measured to be 33 and 67 ms, respectively (Figure 3G). These values are at the lower end among the existing soft pressure sensors summarized in Table S1. As shown in Figure 3H, SHRPSs can output repeatable and stable signals under various cyclic loadings. Compared to their pressure responses (Figures 3Hi and 3Hiii), SHRPSs experienced minor capacitance changes under cyclic stretch (Figure 3Hii) and almost negligible capacitance changes under cyclic bending (Figure 3Hiv). The resistance results corresponding to the capacitance results displayed in Figures 3G and 3Hi are provided in Figures S25A and S25B, respectively. In all cases, the baselines of the signals slightly increase due to the viscoelasticity or some irreversibility of the PNC, which has been widely observed in other reported porous polymeric structures under cyclic loadings.[48,49] We also found that SHRPS was not sensitive to temperature and humidity changes when the CNT doping ratio was below 0.6 wt % (Figures S12 and S13).

Analytical modeling

An analytical model for the hybrid response in SHRPSs is presented, with a multiscale view of the PNC as illustrated in Figure 4A. At the macroscopic level, the piezoresistance of the PNC (R_{PNC}) represents the resistance change due to the enhanced contacts under compression. The piezocapacitance of the air (C_{air}) occurs as the air pores in the PNC deform under pressure. However, when the CNT doping ratio falls in the percolation zone (Figure S14), the microscopic view reveals an additional piezocapacitance within the bulk of the nanocomposite (C_{NC}) where the conductive paths are insufficient. The three piezocomponents (R_{PNC}, C_{NC}, and C_{air}) are connected to three different capacitors of the insulating layer (C_{IL1}, C_{IL2}, and C_{IL3}), as shown in Figure 4B. The overall capacitance of SHRPSs can be calculated based on this equivalent circuit model, as detailed in supplemental experimental procedures 3.

The SHRPS circuit model can degenerate into models of dielectric PNC and fully conductive PNC, which are displayed as insets in Figure 4C and conceptually mentioned in Figure 1C. For sensors with 0 and 0.2 wt % CNTs, which are below the percolation threshold, the dielectric PNC model is appropriate. The fully conductive PNC model is used when C_{NC} and C_{air} are negligible due to highly conductive PNC ligaments. The absolute capacitance of the SHRPS falls between the two extreme cases and increases as the amount of CNT in the PNC increases (Figure 4C). However, after normalization, Figure 4D indicates that 0.4 wt % is the optimal CNT doping ratio that offers the highest pressure sensitivity. This is due to the opposite effects of CNT doping on the dielectric PNC vs. the SHRPS. The fully conductive PNC model shows a lower normalized capacitance change than all SHRPS due to its large initial capacitance and diminishing piezocapacitivity. Thus, the optimal CNT doping ratio emerges at the transition from CPS with dielectric PNC to SHRPS. Figure 4D also reveals that CPSs with fully conductive PNCs and

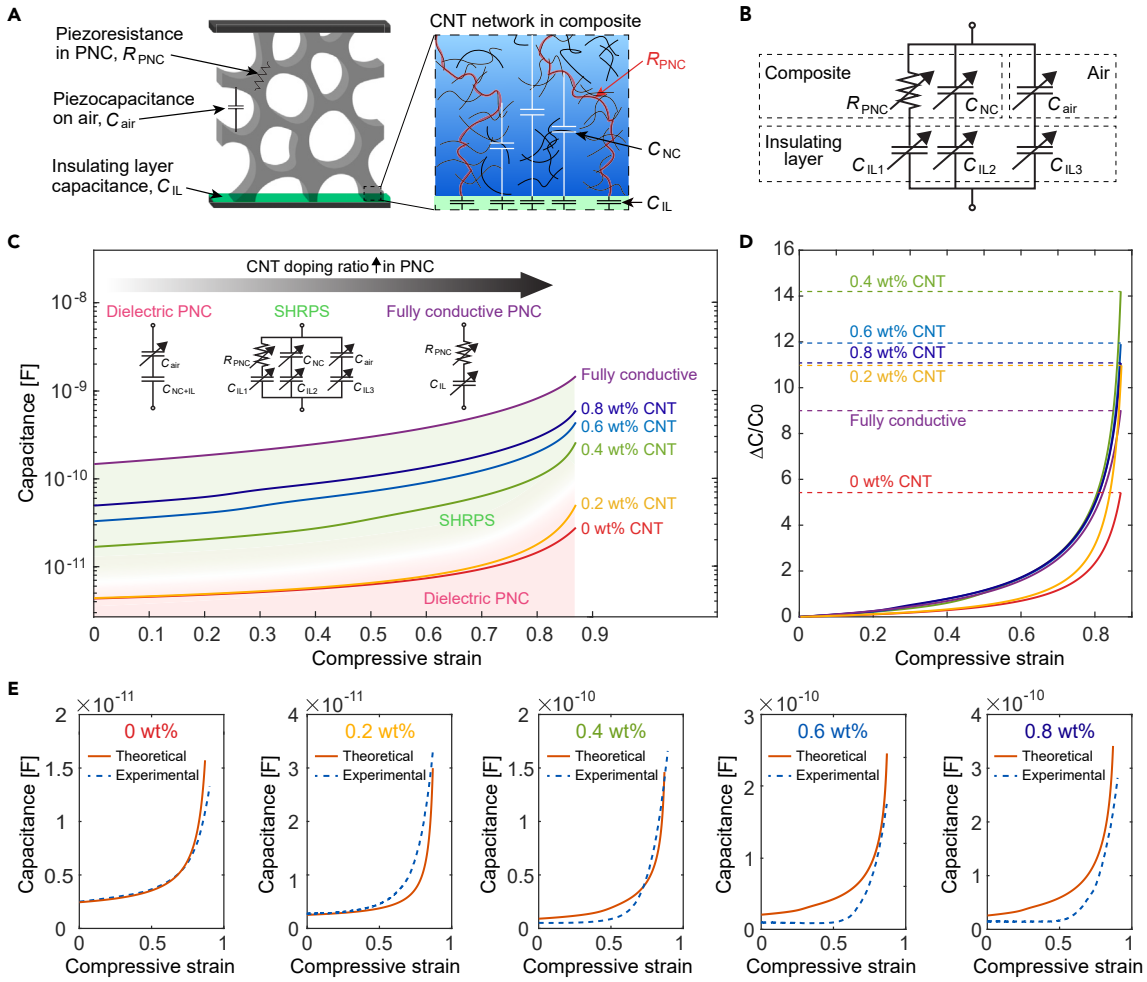

Figure 4. Analytical modeling of SHRPSs

(A) Multiscale schematic representation of the electrical components of SHRPS.

(B) Equivalent circuit of SHRPS.

(C) Theoretical capacitance changes of SHRPS with different CNT doping ratios. Three different equivalent circuits were used depending on the conductivity of the PNC.

(D) Normalized capacitance changes of SHRPS predicted by the model.

(E) Comparison between the theoretical and experimental results of SHRPS with different CNT doping ratios.

dielectric PNCs exhibit the lowest sensitivities due to the absence of hybrid responses.

The theoretical and experimental results are compared in Figure 4E. They agree well over a wide range of compressive strains for all CNT doping ratios. This model represents a significant improvement over our previous model for flexible but non-stretchable HRPSs (Figure S15), which was only accurate for low CNT doping ratios and small applied pressures or compressive strains.[14] This model could also reveal the effects of insulating layer thickness (Figure S16). Although in this work we fixed the AC frequency for the SHRPS impedance measurement to be 1 kHz following the convention of previous CPS research,[13,31] we have performed in-depth theoretical and experimental studies on the effects of AC frequency on HRPSs.[50]

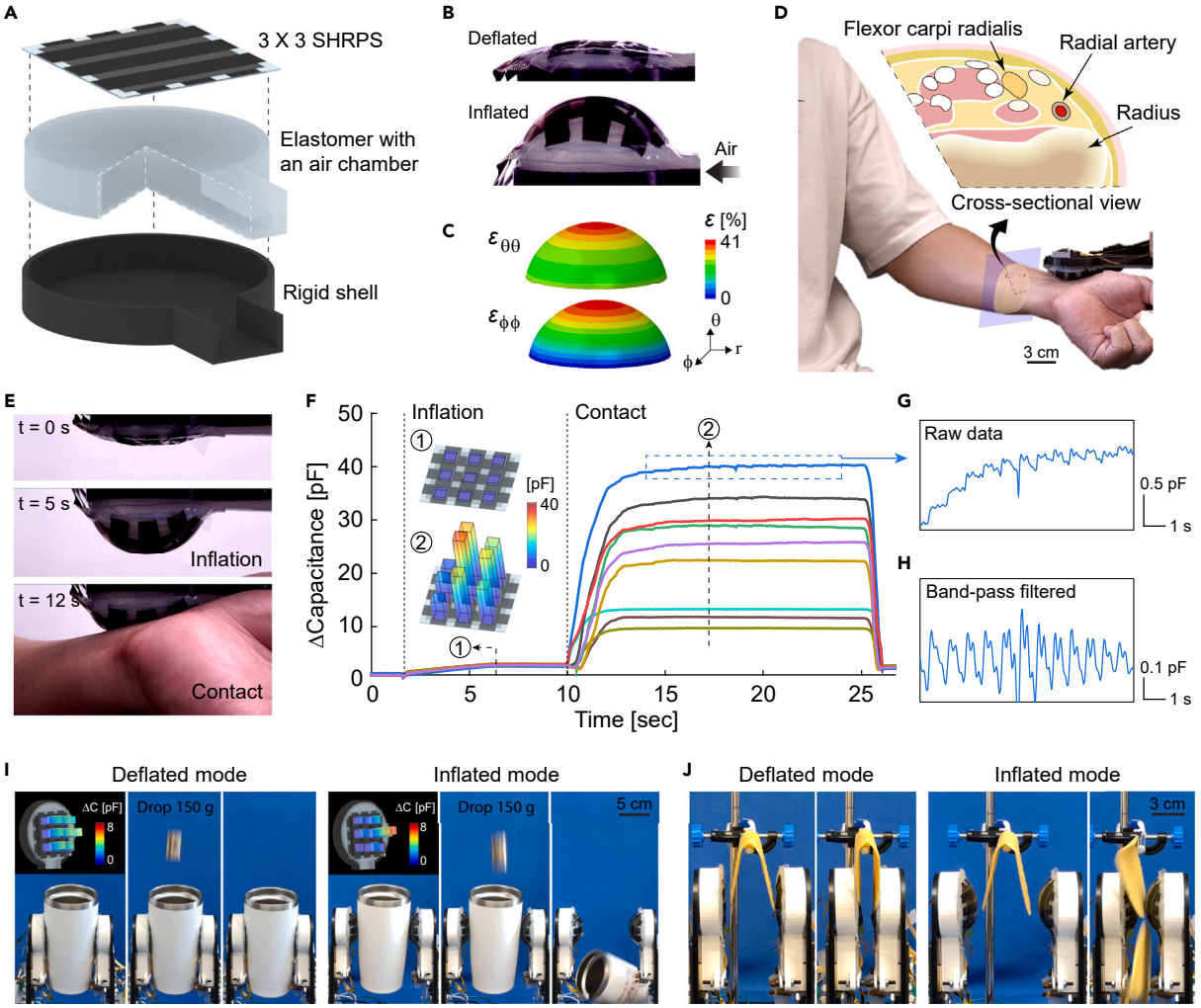

Figure 5. A 3 × 3 array of SHRPSs on a soft inflatable probe

(A) Schematic illustration of the components of the inflatable probe.

(B) The probe in deflated and inflated modes.

(C) Finite element modeling of the tensile strains in the SHRPS under inflation.

(D) Photograph of the measurement of human arterial pulses using the inflated probe, with a cross-sectional illustration of the human wrist.

(E) Snapshots showing the procedure of human radial pulse sensing.

(F) Capacitance changes of 9 SHRPS pixels during the radial artery palpation. The two insets display the pressure distribution before (at 6 s) and after (at 17 s) contacting the wrist.

(G and H) The pulse wave sensed by the central pixel. (G) The raw data and (H) the filtered data.

(I) Gripping a tumbler with a dropped weight using the same force in deflated and inflated modes.

(J) Gripping a brittle taco shell using the same force in deflated and inflated modes.

Demonstrations of SHRPS

Despite several reports on stretchable CPSs applied on soft robots or wearable devices,[18,28,32,51] only one has demonstrated its insensitivity to stretch with a quantified stretch, albeit limited to uniaxial strains up to 15%.[32] To demonstrate SHRPSs' large stretchability and relative insensitivity to stretch, a 3 × 3 SHRPS array was laminated on a soft, inflatable probe as illustrated in Figures 5A and S17, and the corresponding data acquisition circuit was custom designed (Figure S18). Unlike conventional rigid probes that have a fixed geometry and property, this soft probe can adjust its shape (from flat to half-dome, Figure 5B) and stiffness (from 0.07 to 0.36 N/mm, Figure S19) through inflation to suit various

applications. The SHRPS laminated on the inflatable probe exhibits stable capacitance change even with repeated inflation and deflation of the probe (Figure S20). Despite the versatility of inflatable probes,[52] previous CPSs could not be employed on them because inflation induces large biaxial tensile strains up to 40% (Figures 5C and S21), which can cause significant interference with the pressure sensing.

We first demonstrate that an inflated probe is ideal for pulse checking, which requires safe and precise contact on soft human skin. As illustrated in Figure 5D, the radial artery is positioned between the flexor carpi radialis and the radius bones, which are much stiffer than the artery. When a flat probe makes contact with a large area of the wrist, covering bones and tendons, these stiff structures can inhibit adequate preload to the radial artery, as shown in Video S1. In contrast, upon inflation, the capacitance of all SHRPS channels only increases marginally, but when the inflated probe accurately touches the radial artery position (Figure 5E), arterial pulse waveforms are visible in the channel of the central pixel even without amplification or post-data processing (Figures 5F and 5G; Video S2). After applying a 1–4 Hz band-pass filter, typical arterial pulse waveforms[53] are clearly visible, as shown in Figures 5H and S22. Normally, palpation requires accurate alignment between the sensor and the artery; hence, precise positioning of a robotic finger is required.[54] However, the multipixel pressure sensing array on the dome-shaped probe can provide robustness in pulse checking. Even if the first contact fails to detect the pulse, the human subject can simply rotate their wrist to find another pixel that can successfully measure the pulse waves (Video S3). The round shape and soft feel of the inflated probe do not restrict human movement and resemble the touch of human fingers, enabling safe and natural human-robot interaction in the future.

In contrast to the inflated dome-shaped probe, flat and soft grippers are preferred for conformable gripping or gentle manipulations. As depicted in Figure 5I and Video S4, a rigid tumbler was reliably held between two deflated probes while undergoing a weight drop test due to evenly distributed pressure over a large conformable contact area. Conversely, the tumbler fell off during the same weight drop test when gripped by two inflated probes, although the total gripping force was the same. Figure 5J and Video S5 demonstrate that a brittle taco shell can be handled delicately by two deflated probes but will break under the concentrated forces exerted by two inflated probes.

Conclusions

The SHRPS demonstrates a hybrid piezoresistive and piezocapacitive response under pressure but a capacitance-dominant response under stretch. Its high sensitivity to pressure overcomes its sensitivity to stretch, resulting in accurate pressure readings even under stretch. The simple lamination of intrinsically stretchable layers in SHRPSs avoids the complications seen in previous stretchable CPSs. An analytical model was established to understand and predict the hybrid responses of the SHRPS and to shed light on its optimal composition and conditions when hybrid response is lost. The combined high stretchability and high pressure sensitivity of SHRPSs enabled the creation of a smart inflatable probe with adjustable shape and stiffness that is capable of diverse types of tasks. These attributes make SHRPSs a promising candidate for use in e-skin and related fields, such as soft robots and bio-integrated electronics, where mechanical softness and accurate pressure readings under stretch are crucial for human interaction or human integration.

EXPERIMENTAL PROCEDURES

Resource availability

Lead contact

Further information and requests for resources and reagents should be directed to and will be fulfilled by the lead contact, Nanshu Lu (nanshulu@utexas.edu).

Materials availability

This study did not generate new unique materials.

Data and code availability

The authors declare that the data supporting the findings of this study are available within the article and its supplemental information files, as well as from the corresponding author upon reasonable request.

Preparation of PNC

A mixture of hydroxyl functionalized multi-wall CNTs (Carbon Nanotubes Plus) and chloroform (Sigma-Aldrich) was prepared with a ratio of 1 mg CNT:2 mL chloroform. For the 0.2-wt%-CNT-doped PNC, the ratio was 1:3, considering the dilution ratio of Ecoflex in the chloroform. The solution was sonicated by a sonicator (Q500, QSonica) with a power of 500 W for 10 min. Uncured Ecoflex (Ecoflex 00-30, Smooth-On) base polymer prepared by a 1:1 mixing ratio of Ecoflex A and B was then added to the solution according to the target doping ratio of CNT, and the new mixture was sonicated for 10 min. After sonication, the solution was heated and stirred at 100°C and 400 rpm using a magnetic hotplate stirrer (Thermo Scientific) to evaporate the chloroform. When the chloroform-to-Ecoflex weight ratio reached 10:1, a 1-mm-thick nickel foam (TMAX Battery Equipments) was dipped into the solution for 10 s and then extracted with the constant velocity of 0.68 mm/s using an electric motor. The sample was put on a hot plate at 100°C for 10 min and dip coated one more time. The double-dip-coated nickel foam was put in a 150°C oven for 30 min to fully evaporate the chloroform and cure the CNT-Ecoflex composite. The whole specimen was immersed in a 3 M HCl (hydrochloric acid; Sigma-Aldrich) at 80°C for 12 h to etch the nickel foam template. Finally, the PNC was washed with distilled water and then dried using a hot plate at 50°C for 2 h.

Preparation of solid Ecoflex and porous Ecoflex

Solid Ecoflex

Ecoflex was molded in a 1 cm × 1 cm × 1 mm CNC-machined polytetrafluoroethylene (Mcmaster-carr) mold and cured in the oven at 150°C for 30 min.

Porous Ecoflex

A 1-mm-thick nickel foam was dipped twice into a 10:1 diluted Ecoflex by chloroform for 10 s. After that, the curing and etching processes followed that of the PNC.

Electromechanical simulation

Figure 1C's results were obtained through the following simulation procedures. An open-cell foam geometry was conceptually designed to simulate the PNC structure. The finite element method software ABAQUS was employed to simulate the 40% stretching and 40% compression responses of the PNC structure using C3D4H elements. The undeformed and deformed configurations of the PNC were exported from ABAQUS and then imported into COMSOL Multiphysics. Within COMSOL Multiphysics, the PNC configurations were sandwiched between two electrodes with an added insulating layer and air to build a CPS. Three categories of PNCs were considered: dielectric, barely conductive, and fully conductive. For each pressure sensor,

2 V at 1 kHz was applied to the top electrode, and the bottom electrode was grounded. The electric potential and electric fields were simulated across the undeformed, stretched, and compressed configurations with the different PNCs.

Compression test

A Dynamic Mechanical Analyzer (RSA-G2, TA Instruments) was used to control and measure the applied pressure and displacement. The direct current (DC) resistance of the conductive PNC was measured by an electrometer (6514, Keithley), and the impedance of the SHRPS was measured by an LCR meter (3532-50, Hioki) at 1 kHz frequency with a 2 V AC signal in serial mode, both *in situ*.

Stretch test

Customized uniaxial and biaxial stretchers (Figure S4) were used to control tensile strain. The impedance measurement system was used the same way as the compression test.

Sensitivity of reported CPSs

The reported sensitivities of other CPSs are based on different pressure ranges. For a fair comparison of sensitivity within the same pressure range, the sensitivities of other CPSs are extracted based on the slope of a straight line connecting $\frac{\Delta C}{C_0}$ at 0 kPa and $\frac{\Delta C}{C_0}$ at 10 kPa.

Durability test

Compression

The same method for the compression test was used.

Stretch

A hydraulic stretcher (MTS) was used to apply a cyclic tensile strain of 40%.

Bending

An SHRPS was laminated on a 100 μm polypropylene (PP) film (Transferrite, ABI Tape), and the two sides of the PP film were clamped on the hydraulic stretcher (MTS). As the gap between the two clamps decreased by the hydraulic stretcher, the SHRPS on the PP film was bent. The bending radius was measured using recorded images afterward.

Temperature response test

A hot plate (Thermo Scientific) was used to apply heat to the SHRPS. A digital thermometer (TMD-56, Amprobe) with a data logger and USB connection was used to measure the temperature on the top surface of the hot plate. The impedance of the SHRPS was measured by the LCR meter (3532-50, Hioki).

Humidity response test

An SHRPS was positioned within a sealed container, which was connected to a humidifier. The humidifier was controlled to attain a stable humidity level, and a digital humidity sensor (SHT31 Sensirion) was used to monitor the humidity. The impedance of the SHRPS was measured by the LCR meter (3532-50, Hioki).

Measurement system for demonstration

An electrical measurement apparatus was designed to determine the capacitance at each pixel of the 3 × 3 grid-shaped sensor. Impedance was measured by a 12-bit impedance converter (AD5933, Analog Devices) after calibration. Due to the impedance measurement range of the chip, a 3 kHz AC frequency was used to stimulate

external impedance, and the response signals were sampled and digitally converted to impedance data at a sampling rate of 150 Hz. In order to acquire information from multiple channels within the grid, two analog multiplexers (SN74LV4051A, TI) were used to provide row- and column-selection capability. The data were recorded by a nearby PC for post-processing. A block diagram of the measurement system is provided in Figure S18.

Demonstrations of gripping a tumbler and a taco

During the gripping demonstrations (Figures 5I and 5J), a force sensor (FSR01CE, Ohmite) was placed between an inflatable gripper and its rigid backing to ensure the same gripping force was applied in tests with deflated and inflated grippers (Figure S17). Before the experiments, the initial gripper spacing was set at 80 mm. We adjusted the relative air pressure within the soft grippers to be 5 kPa for the inflated mode and 0 kPa for the deflated mode, regulated by a compressed air chamber equipped with a pressure gauge.

Tumbler demonstration

The tumbler has a base diameter of 7.0 cm, a top diameter of 8.6 cm, a height of 16.5 cm, and a weight of 235 g. The following settings were consistently adopted in every drop test whether the tumbler was held by deflated or inflated grippers. Markers were positioned on the tumbler 3.3 cm below the top, guiding the center of the grippers for standardized contact. As the grippers contacted the tumbler, the total contact force, measured by the FSR01CE force sensor, started to increase. The closing of the grippers stopped when the force sensor reached a 1 N setpoint. Subsequently, a 150 g weight was dropped from a height 25.5 cm above the top of the tumbler.

Taco demonstration

A taco shell, with a 7.5 cm radius and a 25° opening, was suspended by a horizontal rod. We ensured consistent contact points by aligning the bottom of the central pixel of the SHRPS with the taco base. The gripper movement ceased when the contact force reached a 0.3 N setpoint.

Repeatability test of SHRPS under biaxial stretch induced by inflation

An inflatable probe with a 3 × 3 SHRPS array was used to test the repeatability of SHRPSs under a cyclic biaxial tensile strain (Figure S20). The internal chamber of the inflatable probe was connected by a tube to a customized pneumatic control system, which consisted of a commercial pressure sensor (ASDXAVX100PGAA5, Honeywell), a solenoid valve (VQ110U-5M, SMC), a mini air pump (12VDC KAS27H), and an Arduino Mega 2560 microcontroller board. The internal pressure in the inflatable probe was measured in real time, and the control system used proportional-integral-derivative control to achieve the desired cyclic inflating/deflating pressure inside the inflatable probe. In each cycle, the inflating and deflating internal pressures were set to 4 and 0 kPa, respectively, and the pressure change was a triangular pressure waveform with a period of 8 s. The impedance of the central pixel sensor of the 3 × 3 SHRPS array was measured by the AD5933 impedance converter and recorded by a PC for analysis.

SUPPLEMENTAL INFORMATION

Supplemental information can be found online at https://doi.org/10.1016/j.matt.2024.04.009.

ACKNOWLEDGMENTS

This research was mainly sponsored by the Cockrell School of Engineering at the University of Texas at Austin. N.L. acknowledges partial support from the US Office

of Naval Research through grant N00014-20-1-2112, the US Army Research Office through Cooperative Agreement no. W911NF-19-2-0333, and the US National Science Foundation through grant ASCENT-2133106.

AUTHOR CONTRIBUTIONS

Conceptualization, K.-H.H., N.L.; methodology, K.-H.H., C.B., S.B., and N.L.; validation, K.-H.H., Z.L., S.K., Z.W., and H.S.; formal analysis, K.-H.H., Z.L., S.K., and Z.W.; investigation, K.-H.H., Z.L., S.K., H.H., Z.W., and H.S.; visualization, K.-H.H., Z.L., and S.K.; resources, N.L.; data curation, K.-H.H.; writing – review & editing, K.-H.H., Z.L., S.K., H.H., Z.W., H.S., and N.L.; writing – original draft, K.-H.H., N.L.; funding acquisition, N.L.; project administration, N.L.; supervision, N.L.

DECLARATION OF INTERESTS

The authors declare no competing interests.

Received: January 30, 2024
Revised: March 19, 2024
Accepted: April 3, 2024
Published: May 1, 2024

REFERENCES

1. Wang, X., Dong, L., Zhang, H., Yu, R., Pan, C., and Wang, Z.L. (2015). Recent progress in electronic skin. Adv. Sci. *2*, 1500169. https://doi.org/10.1002/advs.201500169.

2. Chortos, A., Liu, J., and Bao, Z. (2016). Pursuing prosthetic electronic skin. Nat. Mater. *15*, 937–950. https://doi.org/10.1038/nmat4671.

3. Wang, M., Luo, Y., Wang, T., Wan, C., Pan, L., Pan, S., He, K., Neo, A., and Chen, X. (2021). Artificial skin perception. Adv. Mater. *33*, 2003014. https://doi.org/10.1002/adma.202003014.

4. Kim, Y., Chortos, A., Xu, W., Liu, Y., Oh, J.Y., Son, D., Kang, J., Foudeh, A.M., Zhu, C., Lee, Y., et al. (2018). A bioinspired flexible organic artificial afferent nerve. Science *360*, 998–1003. https://doi.org/10.1126/science.aao0098.

5. Roberts, P., Zadan, M., and Majidi, C. (2021). Soft tactile sensing skins for robotics. Curr. Robot. Rep. *2*, 343–354. https://doi.org/10.1007/s43154-021-00065-2.

6. Pyo, S., Lee, J., Bae, K., Sim, S., and Kim, J. (2021). Recent progress in flexible tactile sensors for human-interactive systems: from sensors to advanced applications. Adv. Mater. *33*, 2005902. https://doi.org/10.1002/adma.202005902.

7. Ha, K.-H., Huh, H., Li, Z., and Lu, N. (2022). Soft Capacitive Pressure Sensors: Trends, Challenges, and Perspectives. ACS Nano *16*, 3442–3448. https://doi.org/10.1021/acsnano.2c00308.

8. Zhou, Y., Zhao, X., Xu, J., Fang, Y., Chen, G., Song, Y., Li, S., and Chen, J. (2021). Giant magnetoelastic effect in soft systems for bioelectronics. Nat. Mater. *20*, 1670–1676. https://doi.org/10.1038/s41563-021-01093-1.

9. Chen, G., Zhao, X., Andalib, S., Xu, J., Zhou, Y., Tat, T., Lin, K., and Chen, J. (2021). Discovering giant magnetoelasticity in soft matter for electronic textiles. Matter *4*, 3725–3740. https://doi.org/10.1016/j.matt.2021.09.012.

10. Mishra, R.B., El-Atab, N., Hussain, A.M., and Hussain, M.M. (2021). Recent progress on flexible capacitive pressure sensors: From design and materials to applications. Adv. Mater. Technol. *6*, 2001023. https://doi.org/10.1002/admt.202001023.

11. Nie, Z., Kwak, J.W., Han, M., and Rogers, J.A. (2022). Mechanically Active Materials and Devices for Bio-Interfaced Pressure Sensors—A Review. Adv. Mater. *2205609*, e2205609. https://doi.org/10.1002/adma.202205609.

12. Lee, G., Kim, H., and Park, I. (2023). A mini review of recent advances in optical pressure sensor. J. Sens. Sci. Technol. *32*, 22–30. https://doi.org/10.46670/JSST.2023.32.1.22.

13. Mannsfeld, S.C.B., Tee, B.C.K., Stoltenberg, R.M., Chen, C.V.H.H., Barman, S., Muir, B.V.O., Sokolov, A.N., Reese, C., and Bao, Z. (2010). Highly sensitive flexible pressure sensors with microstructured rubber dielectric layers. Nat. Mater. *9*, 859–864. https://doi.org/10.1038/nmat2834.

14. Ha, K.H., Zhang, W., Jang, H., Kang, S., Wang, L., Tan, P., Hwang, H., and Lu, N. (2021). Highly Sensitive Capacitive Pressure Sensors over a Wide Pressure Range Enabled by the Hybrid Responses of a Highly Porous Nanocomposite. Adv. Mater. *33*, 2103320. https://doi.org/10.1002/adma.202103320.

15. Yoo, D., Won, D.J., Cho, W., Lim, J., and Kim, J. (2021). Double Side Electromagnetic Interference-Shielded Bending-Insensitive Capacitive-Type Flexible Touch Sensor with Linear Response over a Wide Detection Range. Adv. Mater. Technol. *6*, 2100358. https://doi.org/10.1002/admt.202100358.

16. Boutry, C.M., Negre, M., Jorda, M., Vardoulis, O., Chortos, A., Khatib, O., and Bao, Z. (2018). A hierarchically patterned, bioinspired e-skin able to detect the direction of applied pressure for robotics. Sci. Robot. *3*, eaau6914. https://doi.org/10.1126/scirobotics.aau6914.

17. Kim, H., Kim, G., Kim, T., Lee, S., Kang, D., Hwang, M.S., Chae, Y., Kang, S., Lee, H., Park, H.G., and Shim, W. (2018). Transparent, Flexible, Conformal Capacitive Pressure Sensors with Nanoparticles. Small *14*. https://doi.org/10.1002/smll.201703432.

18. Boutry, C.M., Kaizawa, Y., Schroeder, B.C., Chortos, A., Legrand, A., Wang, Z., Chang, J., Fox, P., and Bao, Z. (2018). A stretchable and biodegradable strain and pressure sensor for orthopaedic application. Nat. Electron. *1*, 314–321. https://doi.org/10.1038/s41928-018-0071-7.

19. Lee, S., Franklin, S., Hassani, F.A., Yokota, T., Nayeem, M.O.G., Wang, Y., Leib, R., Cheng, G., Franklin, D.W., and Someya, T. (2020). Nanomesh pressure sensor for monitoring finger manipulation without sensory interference. Science *370*, 966–970. https://doi.org/10.1126/science.abc973.

20. Qin, J., Yin, L.J., Hao, Y.N., Zhong, S.L., Zhang, D.L., Bi, K., Zhang, Y.X., Zhao, Y., and Dang, Z.M. (2021). Flexible and stretchable capacitive sensors with different microstructures. Adv. Mater. *33*, 2008267. https://doi.org/10.1002/adma.202008267.

21. Rus, D., and Tolley, M.T. (2015). Design, fabrication and control of soft robots. Nature *521*, 467–475. https://doi.org/10.1038/nature14543.

22. Jung, Y.H., Chae, C.W., Vázquez-Guardado, A., Choi, G.E., Lee, H.J., Han, H.J., Park, M., Lim, J., Shin, H.-S., and Su, C.-J. (2022). A wireless haptic interface for programmable patterns of touch across large areas of the skin. Nature Electronics *192*, 1–12. https://doi.org/10.1038/s41928-022-00765-3.

23. Hopkins, M., Vaidyanathan, R., and Mcgregor, A.H. (2020). Examination of the performance characteristics of velostat as an in-socket pressure sensor. IEEE Sensor. J. *20*, 6992–7000. https://doi.org/10.1109/JSEN.2020.2978431.

24. Han, S., Kim, J., Won, S.M., Ma, Y., Kang, D., Xie, Z., Lee, K.-T., Chung, H.U., Banks, A., Min, S., et al. (2018). Battery-free, wireless sensors for full-body pressure and temperature mapping. Sci. Transl. Med. *10*, eaan4950. https://doi.org/10.1126/scitranslmed.aan4950.

25. Shu, L., Hua, T., Wang, Y., Qiao Li, Q., Feng, D.D., and Tao, X. (2010). In-shoe plantar pressure measurement and analysis system based on fabric pressure sensing array. IEEE Trans. Inf. Technol. Biomed. *14*, 767–775. https://doi.org/10.1109/TITB.2009.2038904.

26. Lipomi, D.J., Vosgueritchian, M., Tee, B.C.K., Hellstrom, S.L., Lee, J.A., Fox, C.H., and Bao, Z. (2011). Skin-like pressure and strain sensors based on transparent elastic films of carbon nanotubes. Nat. Nanotechnol. *6*, 788–792. https://doi.org/10.1038/nnano.2011.184.

27. Park, S., Kim, H., Vosgueritchian, M., Cheon, S., Kim, H., Koo, J.H., Kim, T.R., Lee, S., Schwartz, G., Chang, H., and Bao, Z. (2014). Stretchable Energy-Harvesting Tactile Electronic Skin Capable of Differentiating Multiple Mechanical Stimuli Modes. Adv. Mater. *26*, 7324–7332. https://doi.org/10.1002/adma.201402574.

28. Zhang, Y., Liu, S., Miao, Y., Yang, H., Chen, X., Xiao, X., Jiang, Z., Chen, X., Nie, B., and Liu, J. (2020). Highly Stretchable and Sensitive Pressure Sensor Array Based on Icicle-Shaped Liquid Metal Film Electrodes. ACS Appl. Mater. Interfaces *12*, 27961–27970. https://doi.org/10.1021/acsami.0c04939.

29. Sunwoo, S.-H., Ha, K.-H., Lee, S., Lu, N., and Kim, D.-H. (2021). Wearable and Implantable Soft Bioelectronics: Device Designs and Material Strategies. Annu. Rev. Chem. Biomol. Eng. *12*, 359–391. https://doi.org/10.1146/annurev-chembioeng-101420-024336.

30. Larson, C., Peele, B., Li, S., Robinson, S., Totaro, M., Beccai, L., Mazzolai, B., and Shepherd, R. (2016). Highly stretchable electroluminescent skin for optical signaling and tactile sensing. Science *351*, 1071–1074. https://doi.org/10.1126/science.aac5082.

31. Yang, J.C., Kim, J.-O., Oh, J., Kwon, S.Y., Sim, J.Y., Kim, D.W., Choi, H.B., and Park, S. (2019). Microstructured porous pyramid-based ultrahigh sensitive pressure sensor insensitive to strain and temperature. ACS Appl. Mater. Interfaces *11*, 19472–19480. https://doi.org/10.1021/acsami.9b03261.

32. Su, Q., Zou, Q., Li, Y., Chen, Y., Teng, S.-Y., Kelleher, J.T., Nith, R., Cheng, P., Li, N., Liu, W., et al. (2021). A stretchable and strain-unperturbed pressure sensor for motion interference–free tactile monitoring on skins. Sci. Adv. *7*, eabi4563. https://doi.org/10.1126/sciadv.abi4563.

33. Yang, J., Tang, D., Ao, J., Ghosh, T., Neumann, T.V., Zhang, D., Piskarev, Y., Yu, T., Truong, V.K., Xie, K., et al. (2020). Ultrasoft liquid metal elastomer foams with positive and negative piezopermittivity for tactile sensing. Adv. Funct. Mater. *30*, 2002611. https://doi.org/10.1002/adfm.202002611.

34. Zhang, Y., Yang, J., Hou, X., Li, G., Wang, L., Bai, N., Cai, M., Zhao, L., Wang, Y., Zhang, J., et al. (2022). Highly stable flexible pressure sensors with a quasi-homogeneous composition and interlinked interfaces. Nat. Commun. *13*, 1317–1412. https://doi.org/10.1038/s41467-022-29093-y.

35. Zang, Y., Zhang, F., Di, C.-a., and Zhu, D. (2015). Advances of flexible pressure sensors toward artificial intelligence and health care applications. Mater. Horiz. *2*, 140–156. https://doi.org/10.1039/C4MH00147H.

36. Edin, B.B., and Johansson, N. (1995). Skin strain patterns provide kinaesthetic information to the human central nervous system. J. Physiol. *487*, 243–251. https://doi.org/10.1113/jphysiol.1995.sp020875.

37. Cheng, W., Yu, L., Kong, D., Yu, Z., Wang, H., Ma, Z., Wang, Y., Wang, J., Pan, L., and Shi, Y. (2018). Fast-Response and Low-Hysteresis Flexible Pressure Sensor Based on Silicon Nanowires. IEEE Electron. Device Lett. *39*, 1069–1072. https://doi.org/10.1109/LED.2018.2835467.

38. Liu, F., Han, F., Ling, L., Li, J., Zhao, S., Zhao, T., Liang, X., Zhu, D., Zhang, G., Sun, R., et al. (2018). An omni-healable and highly sensitive capacitive pressure sensor with microarray structure. Chem. Eur J. *24*, 16823–16832. https://doi.org/10.1002/chem.201803369.

39. Kwon, D., Lee, T.-I., Kim, M., Kim, S., Kim, T.-S., and Park, I. (2015). Porous dielectric elastomer based ultra-sensitive capacitive pressure sensor and its application to wearable sensing device. High Perform. Dev. IEEE Cornell Conf. 299–302. https://doi.org/10.1109/TRANSDUCERS.2015.7180920.

40. Viry, L., Levi, A., Totaro, M., Mondini, A., Mattoli, V., Mazzolai, B., and Beccai, L. (2014). Flexible three-axial force sensor for soft and highly sensitive artificial touch. Adv. Mater. *26*, 2659. 2614. https://doi.org/10.1002/adma.201305064.

41. Baek, S., Jang, H., Kim, S.Y., Jeong, H., Han, S., Jang, Y., Kim, D.H., and Lee, H.S. (2017). Flexible piezocapacitive sensors based on wrinkled microstructures: toward low-cost fabrication of pressure sensors over large areas. RSC Adv. *7*, 39420–39426. https://doi.org/10.1039/C7RA06997A.

42. Ho, D.H., Sun, Q., Kim, S.Y., Han, J.T., Kim, D.H., and Cho, J.H. (2016). Stretchable and multimodal all graphene electronic skin. Adv. Mater. *28*, 2601–2608. https://doi.org/10.1002/adma.201505739.

43. Shi, H., Al-Rubaiai, M., Holbrook, C.M., Miao, J., Pinto, T., Wang, C., and Tan, X. (2019). Screen-Printed Soft Capacitive Sensors for Spatial Mapping of Both Positive and Negative Pressures. Adv. Funct. Mater. *29*, 1809116. https://doi.org/10.1002/adfm.201809116.

44. Gerratt, A.P., Sommer, N., Lacour, S.P., and Billard, A. (2014). Stretchable Capacitive Tactile Skin on Humanoid Robot Fingers—First Experiments and Results (IEEE), pp. 238–245. https://doi.org/10.1109/HUMANOIDS.2014.7041366.

45. Hu, W., Niu, X., Zhao, R., and Pei, Q. (2013). Elastomeric transparent capacitive sensors based on an interpenetrating composite of silver nanowires and polyurethane. Appl. Phys. Lett. *102*, 38. https://doi.org/10.1063/1.4794143.

46. Wang, X., Li, T., Adams, J., and Yang, J. (2013). Transparent, stretchable, carbon-nanotube-inlaid conductors enabled by standard replication technology for capacitive pressure, strain and touch sensors. J. Mater. Chem. A *1*, 3580–3586. https://doi.org/10.1039/C3TA00079F.

47. Senthil Kumar, K., Chen, P.-Y., and Ren, H. (2019). A review of printable flexible and stretchable tactile sensors. Research. https://doi.org/10.34133/2019/3018568.

48. Si, Y., Wang, L., Wang, X., Tang, N., Yu, J., and Ding, B. (2017). Ultrahigh-water-content, superelastic, and shape-memory nanofiber-assembled hydrogels exhibiting pressure-responsive conductivity. Adv. Mater. *29*, 1700339. https://doi.org/10.1002/adma.201700339.

49. Gong, L., Kyriakides, S., and Jang, W.-Y. (2005). Compressive response of open-cell foams. Part I: Morphology and elastic properties. Int. J. Solid Struct. *42*, 1355–1379. https://doi.org/10.1016/j.ijsolstr.2004.07.023.

50. Li, Z., Ha, K.-H., Wang, Z., Kim, S., Davis, B., Lu, R., Sirohi, J., and Lu, N. (2022). Effects of AC frequency on the capacitance measurement of hybrid response pressure sensors. Soft Matter *18*, 8476–8485. https://doi.org/10.1039/D2SM01250B.

51. Kim, C.-C., Lee, H.-H., Oh, K.H., and Sun, J.-Y. (2016). Highly stretchable, transparent ionic touch panel. Science *353*, 682–687. https://doi.org/10.1126/science.aaf8810.

52. Kuppuswamy, N., Alspach, A., Uttamchandani, A., Creasey, S., Ikeda, T., and Tedrake, R. (2020). Soft-bubble grippers for robust and perceptive manipulation. High Perform. Dev. IEEE Cornell Conf. 9917–9924. https://doi.org/10.1109/IROS45743.2020.9341534.

53. Chen, G., Au, C., and Chen, J. (2021). Textile triboelectric nanogenerators for wearable pulse wave monitoring. Trends Biotechnol. *39*, 1078–1092. https://doi.org/10.1016/j.tibtech.2020.12.011.

54. Billard, A., and Kragic, D. (2019). Trends and challenges in robot manipulation. Science *364*, eaat8414. https://doi.org/10.1126/science.aat8414.